Civil Engineering Dimension
https://ced.petra.ac.id

Numerical Investigation of Seismic Responses of Fault-Crossing Segmental Water Conveyance Tunnel

Primadika, R.A.[1], Fathani, T.F.[1], and Faris, F.[1]*
[1] Department of Civil and Environmental Engineering, Universitas Gadjah Mada, Yogyakarta, INDONESIA

DOI: https://doi.org/10.9744/ced.28.2.145-158

Article Info:
Submitted: Nov 18, 2025
Reviewed: Jan 25, 2026
Accepted: Feb 25, 2026

Keywords:
tunnels,
earthquakes,
faults,
water tunnels,
segmental joints,
dynamic analysis.

Corresponding Author:
Faris, F
Department of Civil and Environmental Engineering, Universitas Gadjah Mada, Yogyakarta, INDONESIA
Email: fikri.faris@ugm.ac.id

Abstract

Tunnels are important infrastructures, but faults and internal water pressure can reduce their seismic performance. These risks are relevant in seismic regions including Indonesia. Although finite element methods are used to analyze tunnel behavior, models with continuous linings overestimate stresses, while the influence of segmental joints remains underexplored. This study investigates the seismic response of the Bener Dam diversion tunnel, Central Java, Indonesia, which crosses an inactive fault and uses segmental lining, using nonlinear time-history finite element analysis. Three scenarios were analyzed: presence versus absence of a fault, empty versus water-filled conditions, and continuous versus jointed linings. The results indicated that fault-crossing tunnels are most vulnerable to horizontal slip, especially under pulse-like earthquakes, with strains concentrated near faults. Water minimally affects deformation but increases internal stress, while segmental joints elevate peak strain yet localize damage. These findings highlighted the need to consider fault, water, and joint effects in seismic tunnel design.

INTRODUCTION

Tunnels play an important role in construction projects and can serve as effective solutions to various engineering problems, for example, in road, railway, and dam projects. In road and railway construction, tunnels enable passage through complex topographical features, such as mountains, which would be expensive to do using conventional methods. In dam construction, tunnels can be utilized to divert river flow during the construction phase or serve as outlets during the operational stage.

One common challenge in tunnel construction is the presence of complex and unavoidable geological conditions. It is not uncommon for tunnels to cross geological structures such as fault fracture zones. These fracture zones can lead to reduced seismic performance of tunnels, even though tunnels generally exhibit better seismic performance than surface structures [1]. Wang [2] stated that most of the heavier tunnel damage during earthquakes also occurred when the tunnel crossed unstable ground, including a ruptured fault plane. Even if the fault is inactive, it can still increase the seismic damage to the tunnel [3].

In addition to geologic structures, water pressure within the tunnel may also contribute to an increase seismic hazard. Previous studies of the seismic response of a pressured water tunnel [4,5], found that the water-filled tunnel suffers higher stresses compared to the empty tunnel. The seismic hazard increases, especially in Indonesia, which has high seismic activity [6].

Note : Discussion is expected before November, 1st 2026, and will be published in the "Civil Engineering Dimension", volume 29, number 1, March 2027.
ISSN : 1410-9530 print / 1979-570X online
Published by : **Petra Christian University**

One way to predict tunnel behavior under seismic events is through the numerical finite element method. The lining is often modeled as continuous, though in reality, tunnels are built in segments with joints, which may lead to overestimating internal stress [7,8]. Several studies [4,9,10], examined flexible joints, but none addressed dowel joints, commonly used in cast-in-place concrete tunnels.

The Bener Dam diversion tunnel in Central Java, Indonesia, is an example of a water tunnel that passes through an inactive fault. A numerical analysis by Bagio et al. [11] examined the fault's impact on the tunnel and concluded that it was safe during excavation but unsafe under seismic loading. However, the study modeled the rock mass as linear-elastic and applied seismic loading using the static-equivalent method, which cannot capture the complex dynamic soil–structure interaction that requires nonlinear dynamic analysis [12]. It also overlooked the effects of internal water pressure and segmental joints on the tunnel's behavior. A nonlinear finite element time-history analysis can capture this complex ground-tunnel interaction, such as demonstrated by Jiao et al. [13], Li et al. [9], and Ghobakhloo et al. [14].

Based on the explanations above, intersections with faults and the presence of water inside tunnels can increase the potential for seismic damage. Modeling a tunnel as continuous also tends to overestimate the internal pressure of the lining, whereas in reality, tunnels are constructed in segments. Therefore, it is important to understand the effects of faults, internal water load, and segmental joints on a tunnel's seismic behavior. However, few studies consider these three factors within a single case. The Bener Dam diversion tunnel, a water conveyance tunnel that crosses a fault and is built with segments, provides a suitable case study. Previous research in the area include flood hazard mapping [15], P-wave measurements [16], geological mapping [17], and the finite element tunnel analysis mentioned earlier [11]. However, no study has examined the seismic response of the diversion tunnel considering fault presence, internal water pressure, and segmental joints using finite element time-history analysis. This research aims to analyze its seismic behavior by incorporating these three factors. The results are expected to improve understanding of seismic tunnel design.

Site Condition

The study site was located in Guntur Village, Purworejo, Central Java. The dam is located at 7°35'54.5" S and 110°1'12.84" E. The geological condition of the site was characterized by monomic breccia, comprising several geological units, including monomic breccia matrix, andesite fragments, tuff fragments, and polymic breccia matrix [18]. Geological structures, especially faults that partially intersect the tunnel path, controlled the quality of the rock mass [17]. An inactive fault was also identified near the tunnel inlet with an orientation of N305°E/87° [11]. The site condition is shown in Figure 1.

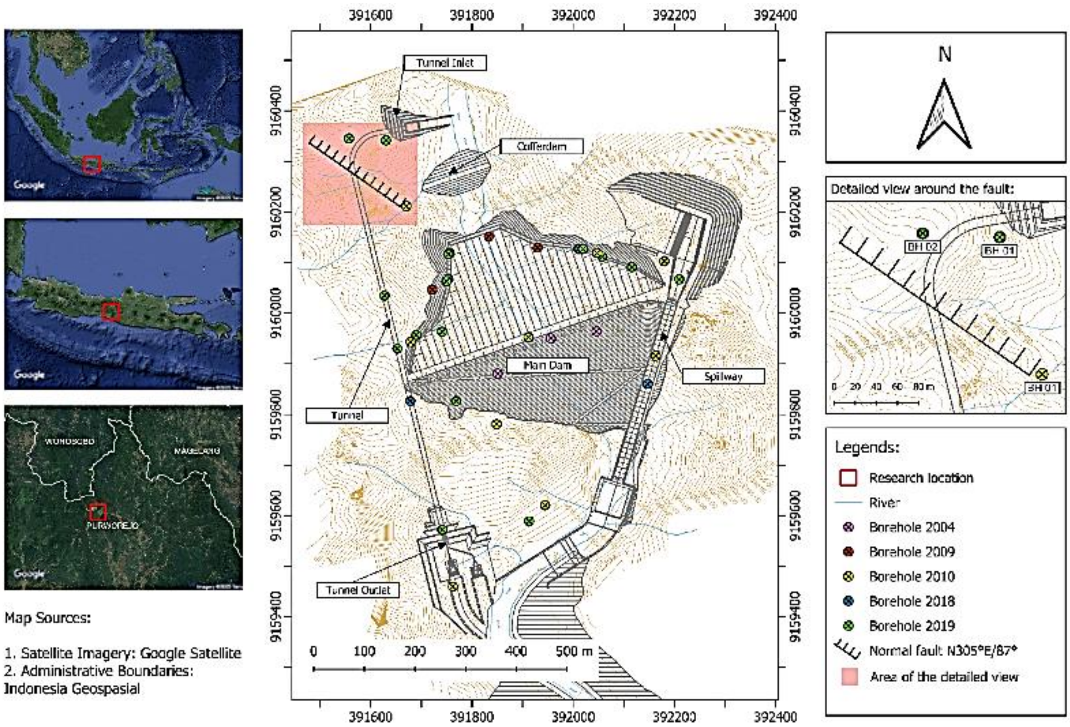

Figure 1. Site Condition [19]

Primadika et al. [19] characterized the rock mass around the tunnel into several layers using the Geological Strength Index (GSI) system [20]. The estimation was based on field investigations conducted by Dharmawan [21] and Bagio [22] on BH 01 and BH 02 of the 2019 borelogs, as well as rock quality measurements by Triristanto [18] on the tunnel faces. The GSI was estimated using empirical correlations introduced by Hoek et al. [23] and Hoek et al. [24]. The GSI values of each layer are shown in Table 1.

Table 1. Layer Simplification and the GSI Values of Each Layer [19]

Depth (m)	GSI value	Rock class	Layer Name for Numerical Model
0 – 2	-	Residual Soil	-
2 – 10	36.64	Poor Rock	Poor Rock
10 – 39	68.10	Good Rock	Good Rock 1
39 – 60	74.00	Good Rock	Good Rock 2
> 60	71.28	Good Rock	Good Rock 3

METHODS

Estimation of Rock Mass and Fault Properties

The required properties for modeling the rock mass are the index properties, stiffness properties, and strength properties. The index properties were obtained from a laboratory test conducted by Dharmawan [21]. The stiffness properties were obtained from analysis by Primadika et al. [19], which estimated the properties based on data from the GSI values and the intact rock properties [21] using formulas from Narimani et al. [25] and Hoek & Diederichs [26].

The strength properties were defined using the generalized Hoek-Brown failure criterion [27], defined by Equations (1) to (4), where $\sigma_1{}'$ is the major principal stress, $\sigma_3{}'$ is the minor principal stress, σ_{ci} is the intact rock uniaxial compressive strength, m_b is the reduced value of the material constant m_i, s and a are the constants for the rock mass, m_i is a value of material constant for intact rock given by the ratio of the σ_{ci} and the tensile strength, and D is the disturbance factor. The value of $m_i = 19$ for breccia rocks [28] and $D = 0$ for excellent quality controlled blasting [27] were used. The σ_{ci} was obtained from a laboratory test by Dharmawan [21].

Other than those parameters, the horizontal to vertical stress ratio (k) was also required. It was estimated using Equation 5 [29], where E is the rock mass elastic modulus and H is the depth below the surface. The estimated rock mass properties are summarized in Table 2.

$$\sigma_1' = \sigma_3' + \sigma_{ci}\left(m_b\frac{\sigma_3'}{\sigma_{ci}} + s\right)^a \tag{1}$$

$$m_b = m_i \exp\left(\frac{\text{GSI} - 100}{28 - 14D}\right) \tag{2}$$

$$s = \exp\left(\frac{\text{GSI} - 100}{9 - 3D}\right) \tag{3}$$

$$a = \frac{1}{2} + \frac{1}{6}\left(e^{\frac{-\text{GSI}}{15}} - e^{\frac{-20}{3}}\right) \tag{4}$$

$$k = 0.25 + 7E\left(0.001 + \frac{1}{H}\right) \tag{5}$$

In Table 2, it can be seen that the value of σ_{ci} of the Poor Rock layer is higher than that of the Good Rock layers. This can occur because the classification of Poor Rock and Good Rock is based on the GSI values, while σ_{ci} can be independent of GSI. The σ_{ci} defines the strength of an intact rock sample, which represents a very small volume compared to the whole rock mass. In contrast, GSI characterizes a whole rock mass based on its geological features. The GSI is then used to reduce the intact rock strength [27], as shown by the relationships in Equations (1) to (4).

The fault was modeled using the discrete discontinuity approach [30] to capture its discontinuity behavior. This method required normal stiffness (K_n) and shear stiffness (K_s) as the stiffness properties, along with cohesion (c) and friction angle (ϕ) as the strength properties, following the Mohr–Coulomb criterion. The values of K_n and K_s were adopted from Primadika et al. [19], derived based on borehole data and the estimation formulas proposed by Rocscience Inc. [31].

Table 2. Estimated Rock Mass Properties

		Poor Rock	Good Rock 1	Good Rock 2	Good Rock 3
Index Properties	Bulk unit weight, γ_b (kN/m^3)	16.000	16.000	17.000	16.000
	Dry unit weight, γ_d (kN/m^3)	15.000	14.000	16.000	15.000
	Saturated unit weight, γ_{sat} (kN/m^3)	18.000	17.000	17.000	18.000
	Void ratio, e	0.850	0.315	0.315	0.489
Stiffness Properties	Elastic modulus, E_{rm} (kPa)	1.95×10^5	2.97×10^6	1.09×10^6	1.33×10^6
	Poisson's ratio, v_{rm}	0.490	0.490	0.490	0.490
Strength Properties	m_b	1.841	6.081	7.507	6.813
	s	0.001	0.029	0.056	0.041
	a	0.516	0.502	0.501	0.501
	σ_{ci} (MPa)	29.814	19.702	13.636	24.452
Horizontal to vertical stress ratio, k		0.330	0.330	0.330	0.330

The strength properties were estimated by first defining the strength using the Hoek-Brown criterion by treating the fault as rock mass, and then converting the parameters into the Mohr-Coulomb criterion. The conversion was done using Equations (6) to (9) [27].

The notation σ'_{cm} is the rock mass uniaxial compressive strength, γ is the rock mass unit weight, and H is the rock mass depth. The tensile strength (σ_t) of the fault was capped at 0 kPa, which is reasonable for high fractured rock mass [32]. After failure, the K_n and K_s were reduced to a value approaching zero to obtain the after-failure behavior. The GSI used to calculate the properties of the fault was estimated as 20, following the recommendation by Marinos et al. [20]. The estimated properties of the fault are summarized in Table 3.

$$\phi' = sin^{-1}\left[\frac{6am_b(s+m_b\sigma_{3n})^{a-1}}{2(1+a)(2+a)+6am_b(s+m_b\sigma'_{3n})^{a-1}}\right] \tag{6}$$

$$c' = \frac{\sigma_{ci}[(1+2a)s+(1-a)m_b\sigma'_{3n}](s+m_b\sigma'_{3n})^{a-1}}{(1+a)(2+a)\sqrt{1+\frac{6am_b(s+m_b\sigma'_{3n})^{a-1}}{(1+a)(2+a)}}} \tag{7}$$

$$\frac{\sigma'_{3max}}{\sigma'_{cm}} = 0.72\left(\frac{\sigma'_{cm}}{\gamma H}\right)^{-0.91} \tag{8}$$

$$\sigma'_{cm} = \sigma'_{ci}\frac{\left(m_b+4s-a(m_b-8s)\right)\left(\frac{m_b}{4}+s\right)^{a-1}}{s(1+a)(2+a)} \tag{9}$$

Table 3. Estimated Properties of the Fault Discontinuity.

Properties	Values
Cohesion, c (kPa)	208.762
Internal friction angle, ϕ (°)	37.053
Tensile strength, σ_t (kPa)	0.000
Normal stiffness, K_n (kPa/m)	2.086×10^4
Shear stiffness, K_s (kPa/m)	7.001×10^3

Fluid-Structure Interaction

Water load inside a structure is often modeled using the added mass approach, but this method can lead to significant error under high-frequency loading [33]. This method also cannot simulate the sloshing behavior of the water during dynamic loading. The most advanced method is by using the Arbitrary Lagrangian-Eulerian method, as conducted by Wang et al. [4]; however, this method requires a large amount of time and computational cost.

A simpler method was introduced by Wilson [33] by modeling the water as a linear-elastic solid material with an extremely low ratio of shear modulus (G) to bulk modulus of water ($\lambda = 300$ ksi) and a Poisson's ratio approaching that of water ($\nu \approx 0.5$). It was recommended to use a ratio of 0.1% or less.

According to the hydraulic analysis by Lestari et al. [34], during the diversion stage, the water flow inside the tunnel is limited to free discharge flow, with a maximum height of around half of the tunnel height. Since the water flow is free discharge only, the approach by Wilson [33] can be considered reasonable and thus used in this study. The approximate properties of water are summarized in Table 4. A value of $G/\lambda = 1 \times 10^{-8}$ was used.

Table 4. Approximate Mechanical Properties of the Water.

Properties	Values
Shear modulus, G (kPa)	2.07×10^{-2}
Poisson's ratio, ν	0.49
Unit weight, γ (kN/m^3)	9.81

Estimation of Segmental Joint Stiffness

The actual tunnel was not designed as a continuous structure. Rather, some joints connect every segment. Modeling the tunnel lining as continuous might overestimate the internal stress that occurs [7]. In this study, the segmental joints were modeled as interface elements with K_n and K_s as stiffness parameters, as conducted by Xiao et al. [35]. The tunnel segments are connected using dowel bars, where one side is set to move in the normal direction freely and the other is embedded inside the concrete. To simulate this, the K_n was set to be very small (0.01 kPa/m). The K_s was estimated by first calculating the dowel deflection using Equations (10) to (13) [36] using a 1 kN load. This deflection can represent a deflection of a dowel in a 1 m^2 area.

$$\Delta = 2y_0 + \delta \tag{10}$$

$$y_0 = \frac{P_t(2+\beta z)}{4\beta^3 E_d I_d} \tag{11}$$

$$\beta = \sqrt[4]{\frac{K_0 d}{4E_d I_d}} \tag{12}$$

$$\delta = \frac{\lambda P_t z}{AG} \tag{13}$$

The notation P_t is the load transferred through the dowel (taken to be 1 kN), β is the relative stiffness of the dowel bar encased in concrete, K_0 is the modulus of dowel support (1.5 million pci is recommended), E_d is the elastic modulus of dowel bar, I_d is the moment of inertia of dowel bar, z is the joint width (6 mm was used), A is the cross sectional area of the dowel bar, G is the shear modulus, and λ is the form factor (10/9 for circular section). Since K_s is the ratio of shear stress (applied force per sectional area) to shear displacement, it can be estimated by Equation (14), where n is the number of dowels in a 1 m^2 area. This approach resulted in a value of $K_s = 1.93 \times 10^5$ kPa/m.

$$K_s = \frac{1}{\Delta} \times n \tag{14}$$

By modeling the joint using interface elements, the normal and shear relative displacements of each segment can be estimated. However, it cannot directly simulate the stress distribution transferred from the embedded dowel to the surrounding concrete. Nevertheless, this method can still represent the dowel's influence on the overall stress distribution of the segment [35].

Input Ground Motions

The input ground motions were based on the criteria in the Indonesian national standard [37], which is a 1000-year return period for tunnels. This corresponds with the Maximum Design Earthquake (MDE) performance level proposed by Wang [2]. The records used here were selected and scaled by Primadika et al. [19] according to the Indonesian national standards [37,38]. The study estimated the shear wave velocity (V_s) of the site using empirical correlations [16,39], which classified the site class as SA. The target spectrum was generated using LINI Bina Marga (lini.binamarga.pu.go.id). The records were obtained from the PEER Ground Motion Database [40] and the NGA Subduction Portal [41]. Due to limited available records, when no record matches the site class, the closest V_S was selected. The response spectra of the selected records are illustrated in Figure 2 and the selected records are summarized in Table 5.

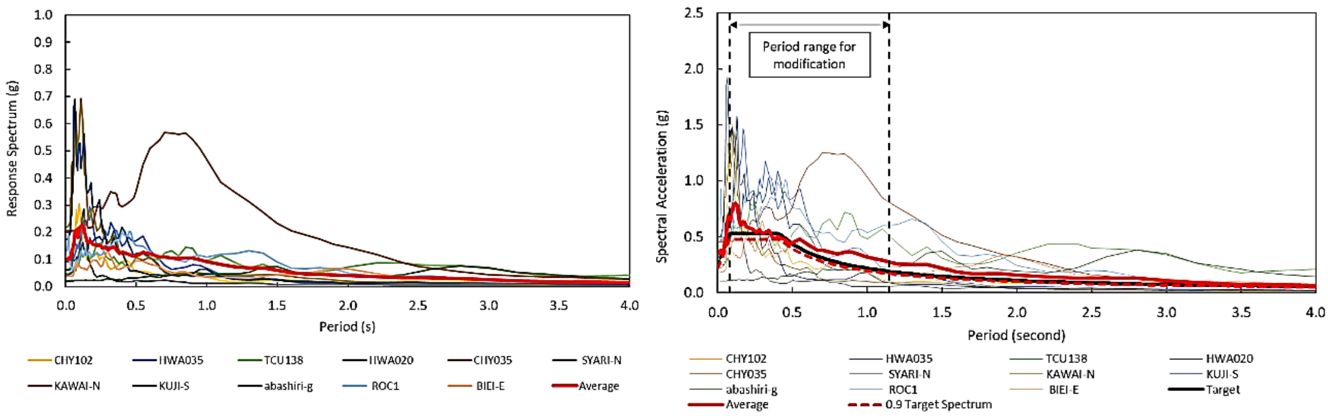

Figure 2. Original Response Spectra (left) and Scaled Spectra (right) of the Selected Records [19]

Table 5. List of Selected Ground Motion and their Scale Factors [19]

No.	Record serial number	Earthquake Name	Year	Station name	Site S-wave velocity, V_s (m/s)	Magnitude, M_w	Distance, R (km)	Earthquake mechanism	Scale factor	Record Source
1.	RSN2753	Chi-Chi Taiwan-04	1999	CHY102	804.36	6.20	39.30	Shallow Crustal	5.0	[40]
2.	RSN3022	Chi-Chi Taiwan-05	1999	HWA035	677.49	6.20	33.57	Shallow Crustal	5.0	
3.	RSN2897	Chi-Chi Taiwan-04	1999	TCU138	652.85	6.20	33.53	Shallow Crustal	5.0	
4.	RSN3008	Chi-Chi Taiwan-05	1999	HWA020	626.43	6.20	34.00	Shallow Crustal	5.0	
5.	RSN2466	Chi-Chi Taiwan-03	1999	CHY035	573.04	6.20	33.86	Shallow Crustal	2.2	
6.	NGAsub RSN4024604	Kushirooki	2004	SYARI-N	517.50	7.01	123.72	Benioff	5.0	[41]
7.	NGAsub RSN4007347	Miyagi_Pre.Off	2011	KAWAI-N	1269.80	7.15	132.60	Benioff	2.1	
8.	NGAsub RSN4022561	SouthSanriku	2003	KUJI-S	966.80	7.03	140.07	Benioff	2.8	
9.	NGAsub RSN4032688	Tokachi-oki	2003	abashiri-g	2229.80	8.29	145.24	Megathrust	5.0	
10.	NGAsub RSN6002233	Coastal.Chile	2015	ROC1	1951.00	8.31	121.84	Megathrust	5.0	
11.	NGAsub RSN4022900	Tokachi-oki	2003	BIEI-E	771.20	8.29	146.69	Megathrust	5.0	

To reduce the analysis time, only the strong duration of the records was used. The modified bracketed method [42] was used to determine the initial point (t_i) of the duration. The termination point (t_t) was determined when the Arias intensity [43] of the record reached 95%. Prism for Earthquake software [44] was used to determine the Arias intensity. Since the earthquakes were applied in both directions, the smallest t_i and the largest t_t of both directions were used. The scaled accelerograms, along with their strong durations, are shown in Figure 3.

Numerical Modeling

The numerical models were constructed using Midas GTS NX. Several models were employed in this study, including one from Primadika et al. [19] that used shell elements to model the tunnel lining. This specific model was used to analyze the 11 ground motions, allowing for the determination of the most significant earthquake. This was done to simplify and speed up the analysis, as shell elements are simpler than solid elements. To understand the tunnels' behavior, more detailed models were then used, which employed solid elements to model the lining.

For all models, the rock mass was modeled as 3D solid elements, the fault was modeled as interface elements [45], the topsoil was modeled as mass elements, and elastic and viscous springs were employed as the boundary conditions [46]. The groundwater level was defined as 9.5 m below the surface, based on the borehole data. The model is illustrated in Figure 4, and the properties of the tunnel lining are summarized in Table 6.

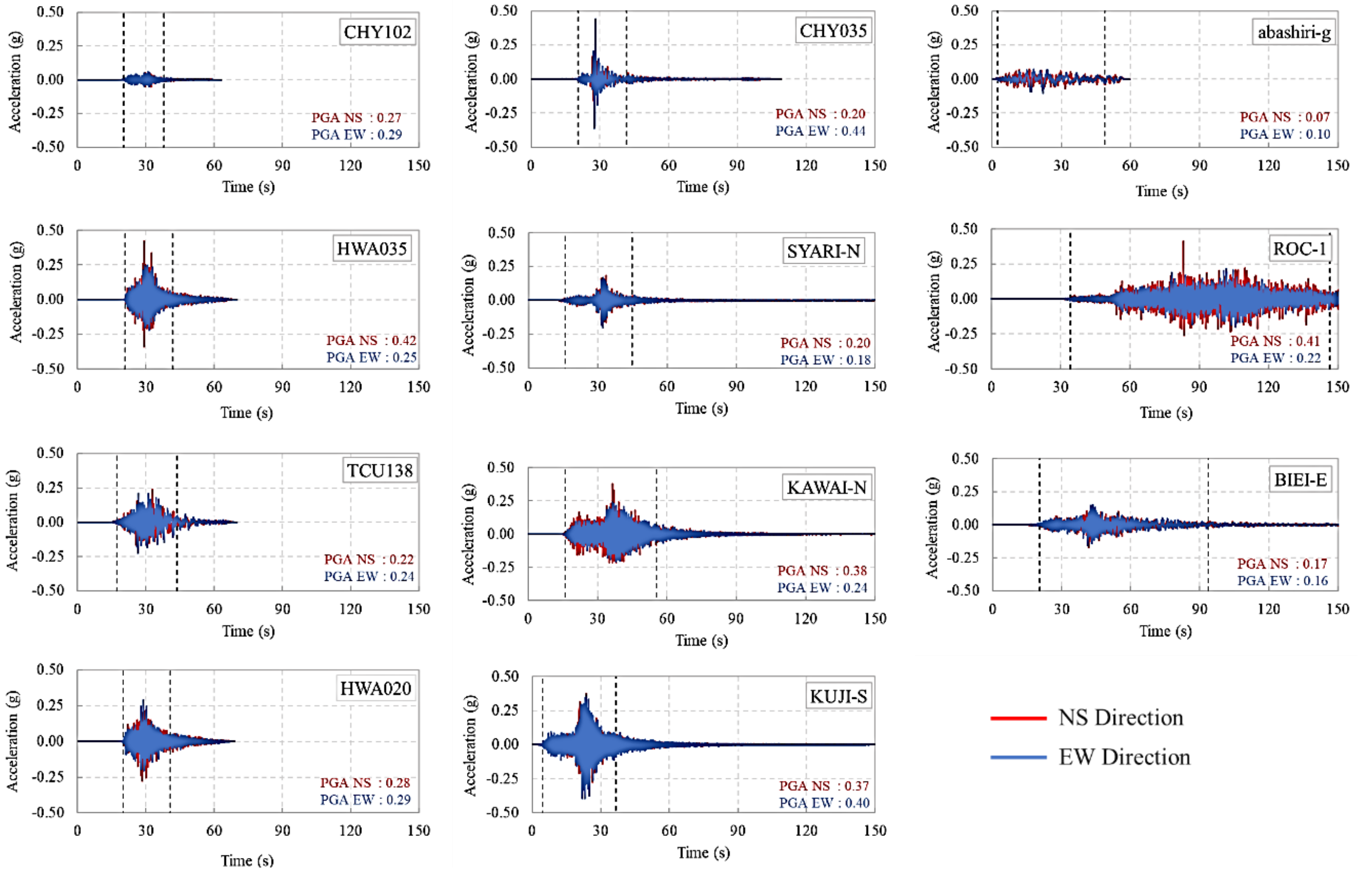

Figure 3. The Scaled Accelerograms and their Strong Durations (Sources Described in Table 5)

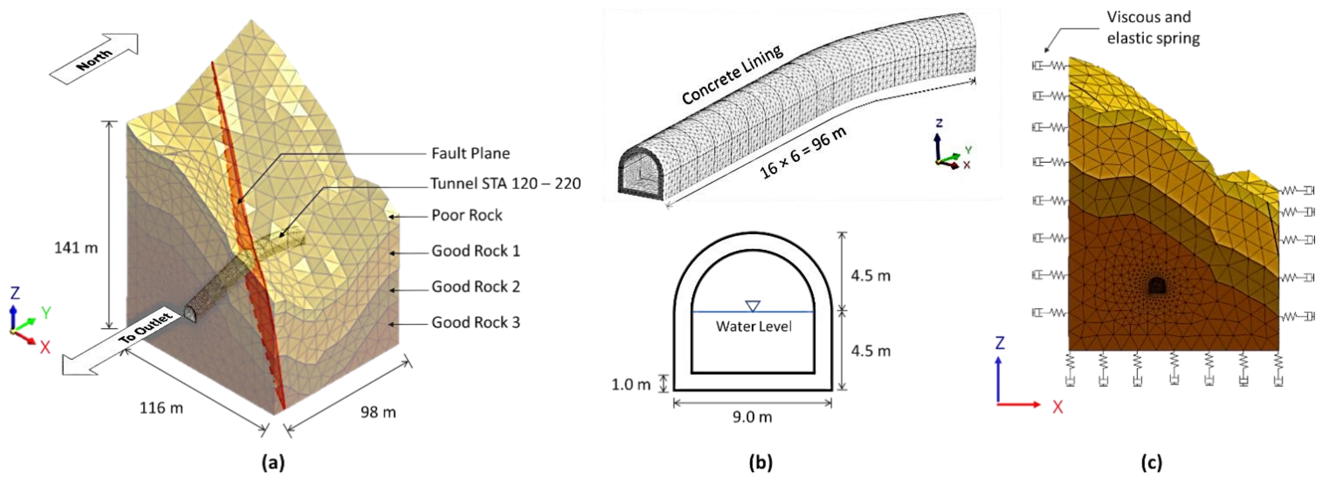

Figure 4. (a) Model Geometry, (b) Lining Geometry, and (c) Model Boundary Conditions

Table 6. Properties of the Tunnel Lining

Parameters	
Strength	Linear elastic
Elastic modulus, E (kPa)	2.03×10^7
Poisson's ratio, ν	0.15
Unit weight, γ (kN/m^3)	24.00

Non-Linear Time History Analysis

Non-linear time history analysis was used to study the seismic response of the tunnel. The gravity loading method was employed to estimate the initial stress of the model. To focus on the earthquake's effect on tunnel deformation, the strains and displacements after the gravity loading in the initial stage were reset to zero. The Rayleigh damping method was implemented to simulate damping in the frequency domain. The damping coefficients were determined based on the first modal period and the period at which 90% of the mass participated. A damping ratio of 0.05 was used.

RESULTS AND DISCUSSION

Seismic Response of the Fault Discontinuity

Fault-crossing tunnels must be designed to withstand the loads caused by fault displacement [1,2]. This highlights the importance of understanding the fault's behavior during earthquakes. Figure 5 shows the response time history of the fault shear displacement. During all earthquakes, the shear displacement increased over time, reached a maximum, then decreased until it eventually stabilized into a permanent deformation. The figure also shows that the maximum shear displacement constantly occurred at the left wall, indicating that in an earthquake scenario, the tunnel was more prone to the fault slip in the horizontal direction.

As shown in Figure 5, the CHY035 earthquake resulted in significantly larger fault shear displacements at all monitoring points. The figure also shows a sudden increase in displacement that occurred only during the CHY035 earthquake. This abrupt rise can be explained by examining the pulse-like characteristics of each quake. The pulse characteristic can be identified by calculating the pulse indicator (PI) [47]. A value of $PI > 0.65$ means the record is pulse-like. The PI values were calculated using SeismoSignal software [48].

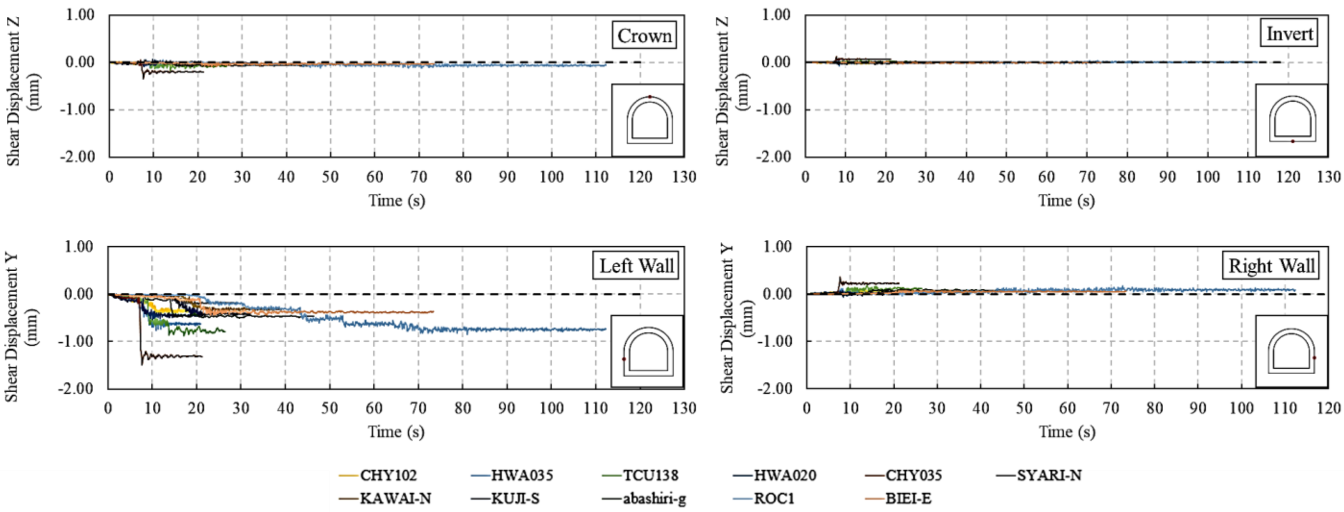

Figure 5. Fault Shear Displacement at Four Monitoring Points of the Fault–Tunnel Intersection

Table 7 shows that only CHY035 exhibits pulse-like features. From this, it can be inferred that earthquakes with pulse-like behavior may pose a greater risk to the tunnel. This aligns with the results from Chen et al. [49], which states that pulse-like loads influence fault movement. It is also consistent with the fact that pulse-like ground motion may increase the risk of earthquake-induced collapse of buildings [50]. Because the CHY035 earthquake produced the largest displacement, it was used as an input load to assess the tunnel response in different scenarios.

Table 7. Pulse-like Characteristic and Maximum Fault Shear Displacement of each Record

No.	Station Name	Pulse Indicator, *PI*	Pulse-Like Characteristics	Fault Shear Displacement (mm)
1.	CHY102	0.48	No	0.44
2.	HWA035	0.41	No	0.77
3.	TCU138	0.46	No	0.88
4.	HWA020	0.35	No	0.54
5.	CHY035	0.72	Yes	1.49
6.	SYARI-N	0.46	No	0.23
7.	KAWAI-N	0.49	No	0.39
8.	KUJI-S	0.39	No	0.48
9.	abashiri-g	0.47	No	0.50
10.	ROC1	0.34	No	0.85
11.	BIEI-E	0.32	No	0.44

Effect of the Fault on the Tunnel's Seismic Responses

To evaluate the impact of the fault on the tunnel, two models were developed: one incorporating the fault and the other without it. The minimum and maximum principal strain response time histories were analyzed to assess the earthquake-induced deformation of the tunnel. The comparison is presented in Figure 6.

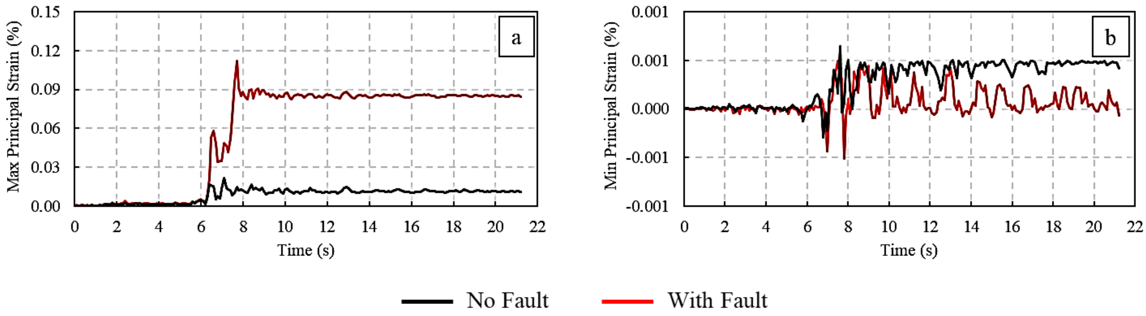

Figure 6. Comparison of the Response Time History of the No-Fault and Fault Models

Figure 6.a shows that the model with the fault produced a much higher maximum principal strain (tension) over time, with values of +0.02% for the model without the fault and +0.11% for the model with the fault. Figure 6.b shows that both models have minimum principal strain values close to zero (around ±0.001%), with the model without the fault retaining more tensile strain. The model with the fault also exhibits greater variability.

To better understand the location that is more vulnerable to fault movement, the principal strain at several monitoring points during the maximum fault movement was evaluated and illustrated in Figure 7. It showed that among all monitoring points of the model with the fault, there are localized increases in principal strains at the fault intersection. This differed significantly from the model's results without the fault. It can also be observed that the strain on the outer side is generally larger, with the largest strain occurring on the left wall, at a value of 0.03%. This indicates that more attention is needed around the fault intersection, for example, by strengthening the segments in this area.

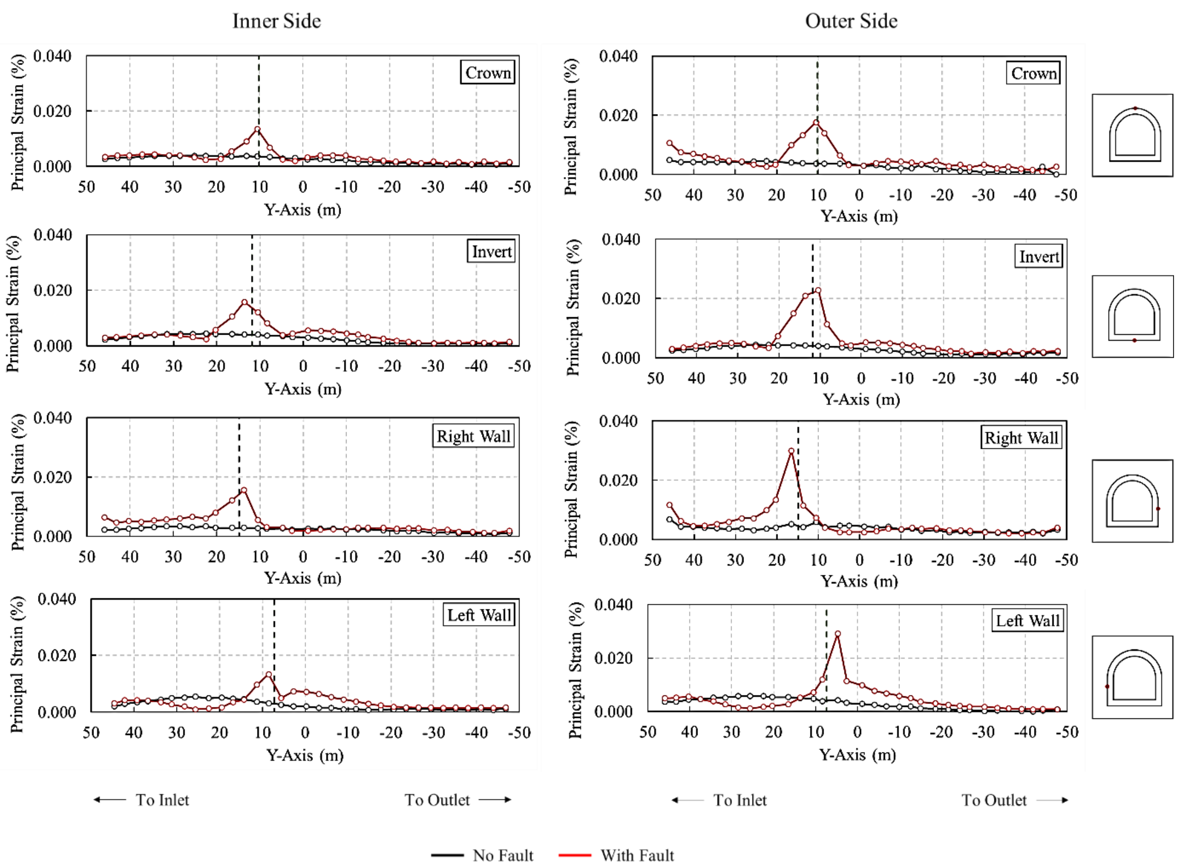

Figure 7. Comparison of Additional Principal Strain along the Tunnel between No-Fault and with Fault Models during Peak Fault Shear Displacement of the CHY035 Earthquake

These results correspond well with Chen et al. [49], which found localized principal stress around the fault intersection of a tunnel crossing an active fault. This is also in agreement with results from Wang et al. [3], Li et al. [9], and Jiao et al. [13], which found that tunnel crossing an inactive fault, when experiencing an earthquake, will produce localized failure around the fault intersection.

Based on the stress value, the no-fault model produced a maximum principal stress of 3.17 MPa compared to the 4.19 MPa of the faulted model. The no-fault model also produced a minimum principal stress of -1.06 MPa compared to the -1.70 MPa of the faulted model. This means that the fault increases both the tension and compression loads experienced by the tunnel due to the combination of self-weight and the earthquake by 32% for tension and 61% for compression loads. Both maximum and minimum principal stress of both models occurred mostly due to the gravity loading stage, but the model with fault remained at a higher stress.

Based on the results above, it can be inferred that the fault significantly affects the tunnel's seismic responses, indicated by the deformation and internal stress. This means the fault needs to be included in the analysis. Not including the fault might cause misinterpretation of the tunnel deformation, which represents the loads received by the tunnel, and lead to errors in identifying critical locations.

Effect of the Water Load on the Tunnel's Seismic Responses

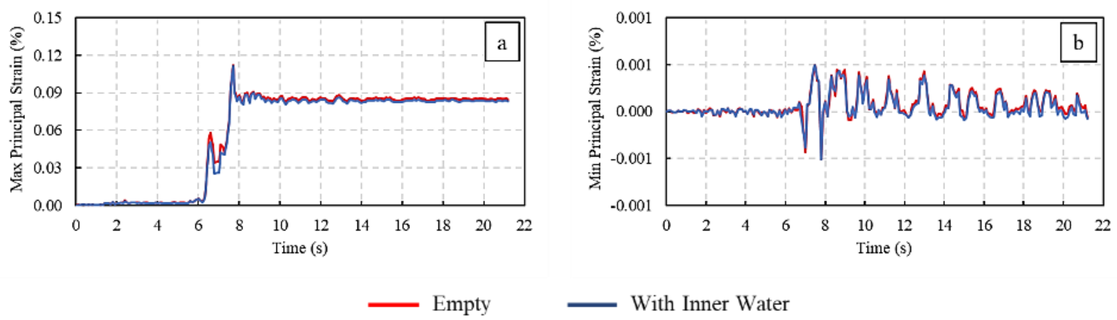

Figure 8. Comparison of the Response Time History of the Empty and Water-filled Models

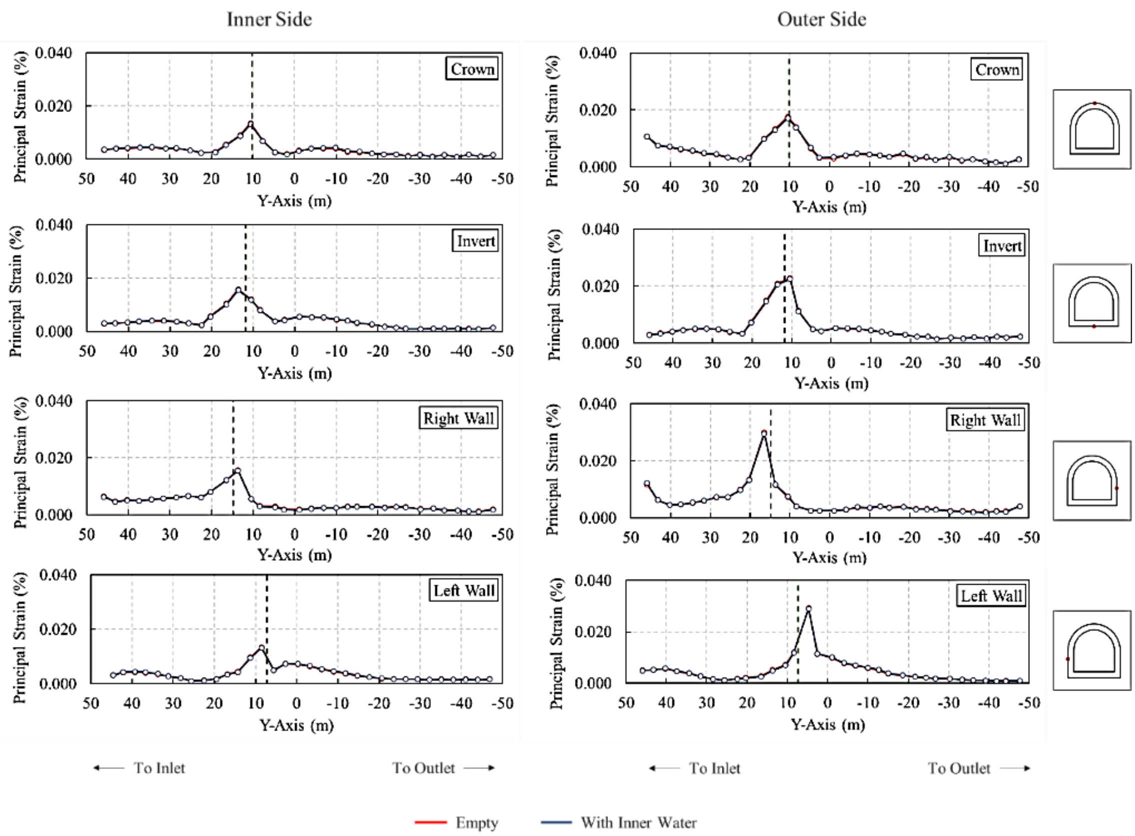

Figure 9. Comparison of Additional Principal Strain along the Tunnel between Empty and Water-filled Models during Peak Fault Shear Displacement of the CHY035 Earthquake

To understand the water load effect, an empty model and a model filled with water were analyzed. The comparison of the principal stress and strain response time history of both models is illustrated in Figure 8. The figure shows that both models exhibited similar behavior with slight differences. Figure 9 illustrates the comparison of the principal strain distribution along the tunnel length of both models. The results show no significant differences between the two models across all monitoring points, with both models exhibiting high localized principal strain at the fault intersection.

Even though both model only shows slight differences in deformation, the model with water produced higher tension and compression, with the maximum value of +4.29 MPa and -2.41 MPa. This means an increase of 2% in tension and 42% in compression, both of which also happened mostly due to the gravity loading stage, but the water-filled model remained at a higher stress. This correlates well with results from Wang et al. [4], which, using the Arbitrary Lagrangian-Eulerian method, find that water load causes an increase in seismic severity of the tunnel. This means the water load should not be ignored in the analysis.

Effect of the Segmental Joint

The effect of segmental joint modeling was also evaluated by comparing the response time history and principal strain distribution between a continuous model and a jointed model. Figure 10 illustrates the comparison of response time histories. Figure 10.a shows that the jointed model produced a higher maximum principal strain, reaching +0.63% compared to +0.11% for the continuous model. Figure 10.b shows that the jointed model exhibited less variability than the continuous model.

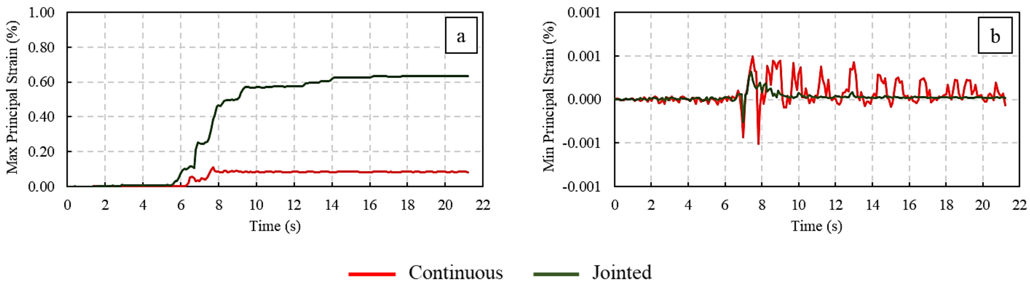

Figure 10. Comparison of the Response Time History of the Continuous and Jointed Models

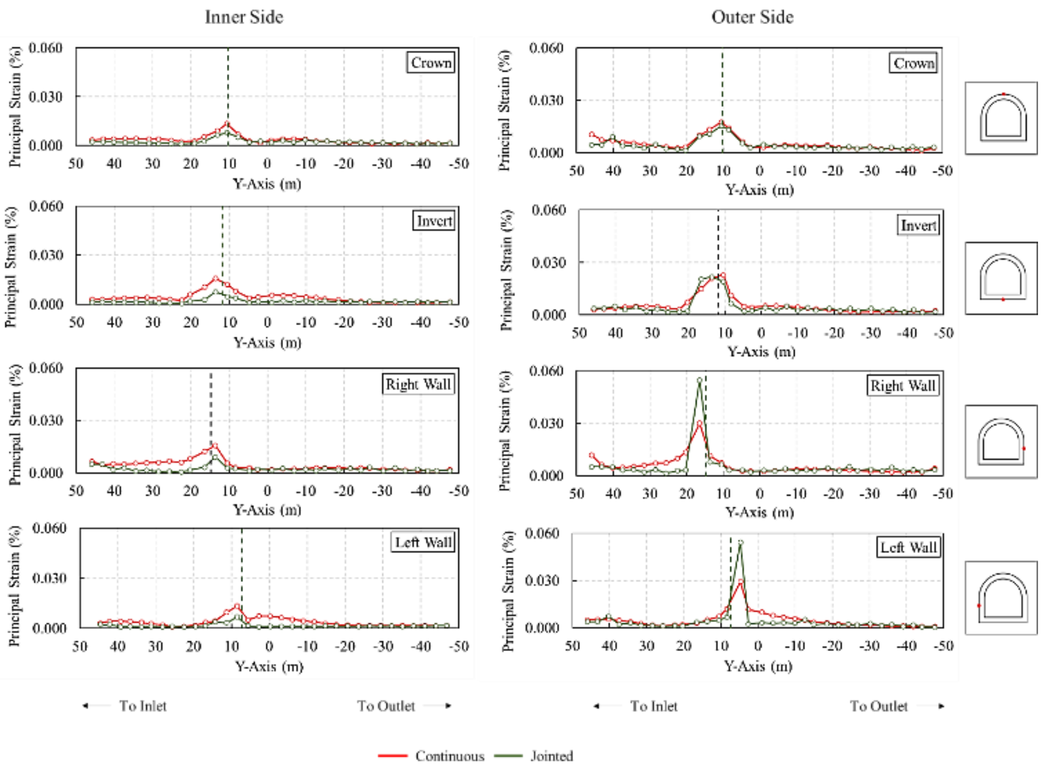

Figure 11. Comparison of Additional Principal Strain along the Tunnel between Continuous and Jointed Models during Peak Fault Shear Displacement of the CHY035 Earthquake

Figure 11 shows the principal strain distribution of both models along the tunnel length. The figure indicates that both models exhibit localized high principal strain at the fault intersection across all monitoring points. On the inner side, the continuous model produced higher principal strains than the jointed model. On the outer side, the crown and invert monitoring points showed almost similar results, with the continuous model slightly higher. A clear difference appears at the wall monitoring points near the fault intersection, where the jointed model produced significantly higher principal strain (around 0.06%) compared to the continuous model (0.03%). Further from the fault intersection, the continuous model tended to produce higher strain.

Based on the stress value, the jointed model produced a maximum principal stress of 4.48 MPa and a minimum principal stress of -2.00 MPa, or an increase of 6.87% in tension and 17.54% in compression. These maximum stresses also mostly due to the gravity loading stage, and the jointed model remained had the higher stress. But, by evaluating the distribution of principal strain in Figure 11, it is apparent that the stress increase is also more localized.

By comparing the results in Figure 10 and Figure 11, it is apparent that although the jointed model produced a higher maximum strain, it is more localized than the continuous model. The higher strain also only happens on the outer side of the walls, while on the other sides, the strain remains consistently lower. This means that the application of a joint may help the tunnel by localizing the damage caused by an earthquake. This behavior is in agreement with the results in Li et al. [9], which found that flexible joints make the failure from an earthquake more localized.

CONCLUSIONS

Based on the results, several key conclusions can be drawn. According to the fault displacements, fault-crossing tunnels are most vulnerable to horizontal fault slip during earthquakes, especially when the earthquake exhibits a pulse-like characteristic. It is also evident that the fault influences the tunnel by increasing the principal strain and internal stress, and also causing a localized increase in strain around the fault intersection. Comparison of empty tunnel and water-filled tunnel showed that the water load caused no significant differences in deformation, but still increased the internal stress of the tunnel, indicating that water load is required in the analysis. The effect of joints generated a higher maximum principal strain and stress, but the increase of strain occurred on the outer side of the walls, while on the other sides, the strain is consistently lower, indicating joint can help minimize the damage by localizing the affected regions. These findings also correlate well with results in previous studies. Overall, these findings highlight the critical role of fault conditions, water load, and segmental joints in accurately assessing and improving the seismic performance of fault-crossing tunnels.

REFERENCES

1. FHWA-NHI-10-034, *Technical Manual for Design and Construction of Road Tunnels - Civil Elements*, National Highway Institute, U.S. Department of Transportation, Federal Highway Administration, Washington, D.C., 2009, retrieved from https://www.fhwa.dot.gov/bridge/tunnel/pubs/nhi09010/tunnel_manual.pdf
2. Wang, J.N., *Seismic Design of Tunnels*, Parsons Brinckerhoff Inc., New York, 1993.
3. Wang, W.L., Wang, T.T., Su, J.J., Lin, C.H., Seng, C.R., and Huang, T.H., Assessment of Damage in Mountain Tunnels due to the Taiwan Chi-Chi Earthquake, *Tunnelling and Underground Space Technology*, 16(3), 2001, pp. 133–150, retrieved from https://doi.org/10.1016/S0886-7798(01)00047-5.
4. Wang, X., Jin, X., Wang, P., and Yang, Z., Parallel Dynamic Analysis of a Large-Scale Water Conveyance Tunnel under Seismic Excitation using ALE Finite-Element Method, *Applied Sciences*, 6(2, Art. no. 2, 2016, retrieved from https://doi.org/10.3390/app6020036.
5. Lyu, D., Yu, C., Ma, S., and Wang, X., Nonlinear Seismic Response of a Hydraulic Tunnel Considering Fluid-Solid Coupling, *Mathematical Problems in Engineering*, 2018(1), 2018, p. 9608542, retrieved from https://doi.org/10.1155/2018/9608542.
6. National Earthquake Study Center of Indonesia, *Earthquake Sources and Hazards Maps of Indonesia 2017,* Ministry of Public Works and Public Housing of the Republic of Indonesia, South Jakarta, Indonesia, 2017. (*In Indonesian*).
7. Ranjbar, G.H., Shahriar, K., and Ahangari, K., Effect of Segmental Joint on Internal Forces in Tunnel Lining under Seismic Loading by Numerical Method, *Journal of Mining and Environment*, 11(3), 2020, pp. 737-751, retrieved from https://doi.org/10.22044/jme.2020.8979.1785.
8. Trad, R., Mroueh, H., Bian, H., and Cormery, F., Synthesis of Numerical Methods for the Design of Segmental Tunnel Lining, *MATEC Web of Conferences*, 295, 2019, p. 03008, retrieved from https://doi.org/10.1051/matecconf/201929503008.

9. Li, R., Yuan, Y., and Zhao, X., Seismic Response of Tunnel across Inactive Fault: Numerical Analysis, *IOP Conference Series: Earth and Environmental Science*, 861(5), 2021, p. 052031, retrieved from https://doi.org/10.1088/1755-1315/861/5/052031.
10. Shahidi, A.R. and Vafaeian, M., Analysis of Longitudinal Profile of the Tunnels in the Active Faulted Zone and Designing the Flexible Lining (for Koohrang-III Tunnel), *Tunnelling and Underground Space Technology*, 20(3), 2005, pp. 213–221, retrieved from https://doi.org/10.1016/j.tust.2004.08.003.
11. Bagio, C.A., Rifa'I, A., and Ismanti, S., Tunnel Stability in Fault Zone Base on 3D Numerical Simulation, *IOP Conference Series: Earth and Environmental Science*, 871(1), 2021, p. 012052, retrieved from https://doi.org/10.1088/1755-1315/871/1/012052.
12. Amrei, S.A.R., Vahdani, R., Gerami, M., and Amiri, G.G., Correlation Effects of Near-Field Seismic Components in Circular Metro Tunnels: A Case Study - Tehran Metro Tunnels, *Shock and Vibration*, 2020(1), 2020, p. 3016465, retrieved from https://doi.org/10.1155/2020/3016465.
13. Jiao, H., Du, X., Zhao, M., Huang, J., Zhao, X., and Ouyang, W., Nonlinear Seismic Response of Rock Tunnels Crossing Inactive Fault under Obliquely Incident Seismic P Waves, *Journal of Earth Science*, 32(5), 2021, pp. 1174–1189, https://doi.org/10.1007/s12583-021-1483-2.
14. Ghobakhloo, E., Pourlak, M., and Razmkhah, A., Seismic Waves Scattering Impact through Tunnel Excavation on Adjacent Monuments Subjected to Far Field Earthquakes, *Civil Engineering Dimension*, 17(2), 2015, pp. 59–66, retrieved from https://doi.org/10.9744/ced.17.2.59-66.
15. Pawestri, M.T., Sujono, J., Istiarto, I., Flood Hazard Mapping of Bogowonto River in Purworejo Regency, Central Java Province, *Journal of the Civil Engineering Forum*, 2(3), 2016, pp. 129-140, retrieved from https://doi.org/10.22146/jcef.24348.
16. Salaamah, A.F., Fathani, T.F., and Wilopo, W., Correlation of P-wave Velocity with Rock Quality Designation (RQD) in Volcanic Rocks, *Journal of Applied Geology*, 3(2), 2019, p. 11, retrieved from https://doi.org/10.22146/jag.48594.
17. Sasangka, D.J., Insani, D., and Indrawan, I.G.B., Engineering Geology Model of Bener Dam Diversion Tunnels in Geological Risk Disaster Mitigation, *Jurnal Geofisika Eksplorasi*, 6(3), 2020, pp. 205–215, retrieved from https://doi.org/10.23960/jge.v6i3.95.
18. Triristanto, E.R., *Engineering Geological Evaluation and Deformation Analysis of the Bener Dam Diversion Tunnel, Purworejo Regency, Central Java Province*, Master Thesis, Gadjah Mada University, Yogyakarta, Indonesia, 2023. (*In Indonesian*).
19. Primadika, R.A., Fathani, T.F., and Faris, F., Modal Analysis and Ground Motion Modification for Tunnel Seismic Design in Fault Zone, *Proceedings of the Simposium Nasional Teknologi Infrastruktur*, Yogyakarta, Indonesia, 2025.
20. Marinos, P.G., Marinos, V., and Hoek, E., Geological Strength Index (GSI). A Characterization Tool for Assessing Engineering Properties for Rock Masses, In: Ollala, C., Perucho, Á., Romana, M., Editors, *Underground Works under Special Conditions: Proceedings of the ISRM Workshop W1, Madrid, Spain, 6-7 July* 2007, Taylor & Francis, 2007, retrieved from https://doi.org/10.1201/NOE0415450287.
21. Dharmawan, A.G., *Evaluation of Engineering Geological Conditions and Stability Analysis of the Bener Dam Diversion Tunnel, Purworejo Regency, Central Java Province*, Master Thesis, Gadjah Mada University, Yogyakarta, Indonesia, 2019. (*In Indonesian*).
22. Bagio, C.A., *Analysis of the Effect of Fault Existence on Tunnel Stability Based on 3D Numerical Simula*tion, Master Thesis, Gadjah Mada University, Yogyakarta, Indonesia, 2021. (*In Indonesian*).
23. Hoek, E., Carter, T.G., and Diederichs, M.S., Quantification of the Geological Strength Index Chart, *Proceedings of the 47th U.S. Rock Mechanics/Geomechanics Symposium*, 2013, p. ARMA-2013-672.
24. Hoek, E., Kaiser, P.K., and Bawden, W.F., *Support of Underground Excavations in Hard Rock*, 1995.
25. Narimani, S., Davarpanah, S.M., and Vásárhelyi, B., Estimation of the Poisson's Ratio of the Rock Mass, *Periodica Polytechnica Civil Engineering*, 68(1), 2023, pp. 274–288, retrieved from https://doi.org/10.3311/PPci.22689.
26. Hoek, E. and Diederichs, M.S, Empirical Estimation of Rock Mass Modulus, *International Journal of Rock Mechanics and Mining Sciences*, 43(2), 2006, pp. 203–215, retrieved from https://doi.org/10.1016/j.ijrmms.2005.06.005.
27. Hoek, E., Carranza-Torres, C., and Corkum, B., Hoek-Brown Failure Criterion - 2002 Edition, *Proceedings of the NARMS-TAC Conference*, Toronto, 2002.
28. Marinos, P. and Hoek, E., GSI: A Geologically Friendly Tool for Rock Mass Strength Estimation, *Proceedings of the ISRM International Symposium*, 2000.
29. Sheorey, P.R., A Theory for In Situ Stresses in Isotropic and Transversely Isotropic Rock, *International Journal of Rock Mechanics and Mining Sciences & Geomechanics Abstracts*, 31(1), 1994, pp. 23–34, reterieved from https://doi.org/10.1016/0148-9062(94)92312-4.

30. Leijon, B. and Conterra, A.B., *Mechanical Properties of Fracture Zones*, Swedish Nuclear Fuel and Waste Management Co., Stockholm, 1993, retrieved from https://skb.se/publikation/9263/TR93-19_OCR.pdf.
31. Rocscience Inc., *Estimating Joint Stiffness*, accessed: Feb. 01, 2025, retrieved from https://static.rocscience.cloud/assets/verification-and-theory/RS2/RS2-Estimating-Joint-Stiffness.pdf.
32. Hoek, E., Strength of Jointed Rock Masses, *Géotechnique*, 33(3), 1983, pp. 187–223, retrieved from https://doi.org/10.1680/geot.1983.33.3.187.
33. Wilson, E.L., *The 2005 Version of Three Dimensional Static and Dynamic Analysis of Structures*, 2005, retrieved from https://edwilson.org/bookshelf/2005ver.
34. Lestari, Y., Istiarto, I., and Sujono, J., Performance of Dodging Channels and Cofferdams against Flood Flows in the Construction of Bener Dam, *Inersia: Jurnal Teknik Sipil dan Arsitektur*, 19(2), Art. no. 2, 2023, retrieved from https://doi.org/10.21831/inersia.v19i2.58182.
35. Xiao, X., Wang, J., Wang, J., and Zhou, H., Determination of Local Stiffness for the Joint of Tunnel Lining in the Simulation, *Revista Internacional de Métodos Numéricos para Cálculo y Diseño en Ingeniería*, 40(2), 2024, retrieved from https://doi.org/10.23967/j.rimni.2024.03.005.
36. FHWA-HRT-06-106, *Design and Evaluation of Jointed Plain Concrete Pavement with Fiber Reinforced Polymer Dowels*, U.S. Department of Transportation, Federal Highway Administration, Washington, D.C, 2009, retrieved from https://www.fhwa.dot.gov/publications/research/infrastructure/pavements/06106/chap6.cfm
37. SNI 8460:2017, *Geotechnical Design Requirements*, National Standardization Agency of Indonesia, 2017. (*In Indonesian*).
38. SNI 8899:2020, *Procedures for Selecting and Modifying Surface Ground Motion for Earthquake-Resistant Building Planning*, National Standardization Agency of Indonesia, 2020. (*In Indonesian*).
39. Wyering, L., Villeneuve, M., and Wallis, I., The Effects of Hydrothermal Alteration on Mechanical Rock Properties of the Andesite Breccia and Tahorakuri Formation from the Ngatamariki Geothermal Field, New Zealand and Empirical Relations between Rock Strength and Physical Properties, *Proceedings of the 34th New Zealand Geothermal Workshop*, Auckland, New Zealand, 2012.
40. The Pacific Earthquake Engineering Research Center, *PEER Ground Motion Database - PEER Center*, accessed: Sep. 04, 2025, retrieved from https://ngawest2.berkeley.edu/.
41. Mazzoni, S., NGA-Subduction Portal: Ground-motion Record Selection and Download, *The B. John Garrick Institute for the Risk Sciences*, 2022, retrieved from https://doi.org/10.34948/N3D59V.
42. He, Y., Li, S., Wei, Y., and Xie, L., A Novel Strong Ground Motion Duration to Reduce Computation Time of Structural Time History Analysis, *Soil Dynamics and Earthquake Engineering*, 164, p. 107641, 2023, retrieved from https://doi.org/10.1016/j.soildyn.2022.107641.
43. Arias, A., Measure of Earthquake Intensity, in: Hansen, R.J., Editor, *Seismic Design for Nuclear Power Plants*, Massachusetts Institute of Technology Press, 1970, pp. 438–83, retrieved from https://www.osti.gov/biblio/4167721.
44. Earthquake Engineering Research Group INHA University, *PRISM - Program for Earthquake Response Spectra*, accessed: Jun. 26, 2025, retrieved from https://sem.inha.ac.kr/prism_2021/index.htm.
45. Midas IT Co., *Interface*, accessed: May 04, 2025, retrieved from https://manual.midasuser.com/en_common/gts%20nx/150/GTS_NX/Mesh/Property,Coordinate,Function/Material/General_Material(Behavioral_properties)/Interface.htm.
46. Midas IT Co., *Transmitting*, accessed: May 08, 2025, retrieved from https://manual.midasuser.com/en_common/feanx/340/FEA_NX/Dynamic_Analysis/Boundary/Transmitting.htm.
47. Kardoutsou, V., Taflampas, I., and Psycharis, I.N., A New Pulse Indicator for the Classification of Ground Motions, *Bulletin of the Seismological Society of America*, 107(3), 2017, pp. 1356–1364, https://doi.org/10.1785/0120160301.
48. Seismosoft, *SeismoSignal - Strong-Motion Data Processing*, accessed: Jan. 29, 2026, retrieved from https://seismosoft.com/products/seismosignal/.
49. Chen, P., Geng, P., Chen, J., and Gu, W., The Seismic Damage Mechanism of Daliang Tunnel by Fault Dislocation during the 2022 Menyuan Ms6.9 Earthquake based on Unidirectional Velocity Pulse Input, *Engineering Failure Analysis*, 145, 2023, p. 107047, retrieved from https://doi.org/10.1016/j.engfailanal.2023.107047.
50. Liel, A. and Champion, C., *The Effect of Near-Fault Directivity on Building Seismic Collapse Risk*, U.S. Geological Survey, Feb. 2010, retrieved from https://earthquake.usgs.gov/cfusion/external_grants/reports/G10AP00041.pdf.